ADVANCED OPTICAL MATERIALS
www.advopticalmat.de

Optical Momentum Alignment Effect in WSe_2 Phototransistor

*Yuchen Zhang and Ya-Qiong Xu**

The optical momentum alignment effect is demonstrated in WSe_2 phototransistors . When the photon energy is above the A exciton energy, the maximum photocurrent response occurs for the light polarization direction parallel to the metal electrode edge, suggesting that electrons in the valence band of WSe_2 prefer to absorb photons with the polarization direction perpendicular to their momentum direction. Further studies indicate that the anisotropic distribution of photo-excited carriers is likely due to the pseudospin-induced optical transition selection rules. If the photon energy is below the A exciton energy, the photocurrent signals are maximized when the incident light is polarized in the direction perpendicular to the electrode edge, which is mainly attributed to the polarized absorption of the plasmonic gold electrodes. Moreover, the photocurrent peak can be controlled by an electric field via the quantum confined Stark effect. This resonance peak can also be shifted by adjusting environmental temperatures due to the temperature-dependent nature of the WSe_2 band gap. These experimental studies shed light on the knowledge of photocurrent generation mechanisms, opening the door for engineering future anisotropic optoelectronics.

1. Introduction

2D transition metal dichalcogenides (TMDs) have gained significant interests duo to their unique electronic and optoelectronic properties.[1–3] Monolayer or few-layer TMDs can be separated from bulk materials and transferred onto substrates via high-quality mechanical exfoliation, owing to the weak van der Waals interlayer interactions. With reduced layers, some TMDs tend to transform from indirect to direct band gap materials with increased band gaps.[4] For instance, WSe_2 has a direct band gap (≈1.7 eV) in the monolayer form, and gradually decreases its band gap with increased thickness.[5,6] Moreover, recent studies have shown that the strong spin–orbit interactions in TMDs lead to a giant split of the valence band that in turn allows for valley-selective excitation at the K and K′ points,[7–9] which are located at the corners of the hexagonal Brillouin zone. For single- and bi-layer WSe_2, the optical transition at the K and K′ points can only be excited by the right-handed circularly polarized light σ^+ and left-handed circularly polarized light σ^-, respectively. Furthermore, the valley-induced emission peaks in TMDs can be modulated by either an external electric field or environmental temperature.[10–12] The former is likely due to the quantum confined Stark effect, a fundamental phenomenon for low-dimensional materials.[13] The latter may result from the temperature-dependent nature of TMD band gaps.

Although considerable research has been devoted to the valley-dependent selection rule of single- and bi-layer TMDs in their photoluminescence studies, rather less attention has been paid to explore their photocurrent generation mechanisms under linearly polarized excitation. In fact, photoresponses generated by linearly polarized incident light in conventional semiconductors have been intensively studied for decades, where the optical momentum alignment effect is believed to play an important role in the polarization of photoresponses.[14,15] For example, anisotropic momentum distribution of photo-induced carriers has been shown in GaAs under interband excitation, which mainly originates from the optical selection rules for heavy-hole and light-hole bands at the Γ point.[14] The momentum anisotropy of photo-induced carriers has also been demonstrated in GaN-based 2D electron gas through photocurrent measurements.[15] Recently, graphene and graphene-like gapped 2D Dirac materials are theoretically predicated to have a strongly anisotropic distribution of photo-excited carriers under linearly polarized excitation due to the pseudospin-induced optical transition selection rules.[16] Therefore, it will be important to explore how linearly polarized excitation influences photocurrent generation in TMDs.

Here, we investigate the photocurrent generation mechanisms in WSe_2 phototransistors under linearly polarized excitation. When the photon energy is above the A exciton energy, the photocurrent signals at WSe_2-metal junctions reach maximum if the incident light polarization is parallel to the metal electrode edge or perpendicular to the momentum direction of electrons. Such anisotropic distribution of photo-excited carriers is likely due to the pseudospin-induced optical transition selection rules. This is known as the optical momentum

Y. Zhang, Prof. Y.-Q. Xu
Department of Electrical Engineering and Computer Science
Vanderbilt University
Nashville, TN 37235, USA
E-mail: yaqiong.xu@vanderbilt.edu
Prof. Y.-Q. Xu
Department of Physics and Astronomy
Vanderbilt University
Nashville, TN 37235, USA
The ORCID identification number(s) for the author(s) of this article can be found under https://doi.org/10.1002/adom.202002243.

DOI: 10.1002/adom.202002243

alignment effect in conventional semiconductors.[14] When the photon energy is below the A exciton energy, the photocurrent intensity reduces significantly and reaches its maximum when the incident light polarization is perpendicular to the metal electrode edge, owing to hot electron injection induced by the surface plasmonic effect of gold electrodes. Moreover, we find that when an external electric field is applied, the photocurrent peak can be shifted due to the quantum confined Stark effect. We also demonstrate that the exciton energy can be modulated by the temperature since the band gap of WSe_2 depends on the temperature. To the best of our knowledge, it is the first time to demonstrate optical momentum alignment effect induced linearly polarized photocurrent response in WSe_2 phototransistors. In the past few years, substantial efforts have been made to improve the photoresponsivities and speeds of TMD-based devices,[17–23] while limited researches focus on their linearly polarized properties since they are isotropic. Our studies of the anisotropic photocurrent generation mechanisms help understanding the basic properties of TMDs and broaden the horizon for future TMD-based anisotropic optoelectronics.

2. Results and Discussion

Figure 1a shows the schematic diagram of a WSe_2 transistor, in which a WSe_2 flake was mechanically exfoliated from its bulk crystal and subsequently transferred onto a degenerately doped silicon substrate covered with a 300 nm thick thermal SiO_2 layer. Optical microscopy was utilized to identify thin WSe_2 flakes, whose thicknesses were inspected by atomic force microscope (AFM) and Raman spectroscopy. Figure 1b shows a typical Raman spectrum of few-layer WSe_2, where strong E^1_{2g} (251.2 cm^{-1}) and A_{1g} A_{1g}(263.5 cm^{-1}) modes of WSe_2 are detected. A peak near 308 cm^{-1} (B^1_{2g}) is also observed, which is a marker for few-layer WSe_2.[24] Source and drain metal electrodes were then fabricated on top of WSe_2 flakes by standard electron beam lithography and subsequent deposition of 5 nm Cr and 40 nm Au. The degenerately doped Si substrate was used as the back gate. To explore the exciton dynamics of WSe_2, we performed spatially resolved scanning photocurrent measurements in a Janis ST-500 microscopy cryostat under high vacuum (≈10^{-6} Torr). Figures 1c and 1d show the reflection and photocurrent images of a few-layer WSe_2 transistor at a zero drain-source bias under 650 nm illumination, respectively. Remarkable photocurrent signals are located at WSe_2-metal junctions, where the built-in electric field induced by Schottky barriers can dissociate photo-excited electron–hole pairs (EHPs) efficiently, leading to photocurrent responses.

To investigate photocurrent generation mechanisms, we performed wavelength-dependent photocurrent measurements. As shown in **Figure 2**a, there is a photocurrent peak located around 755 nm (≈1.64 eV), which is corresponding to the A exciton resonance for few-layer WSe_2.[25] We also find that when the photon energy is above the A exciton energy, the maximum

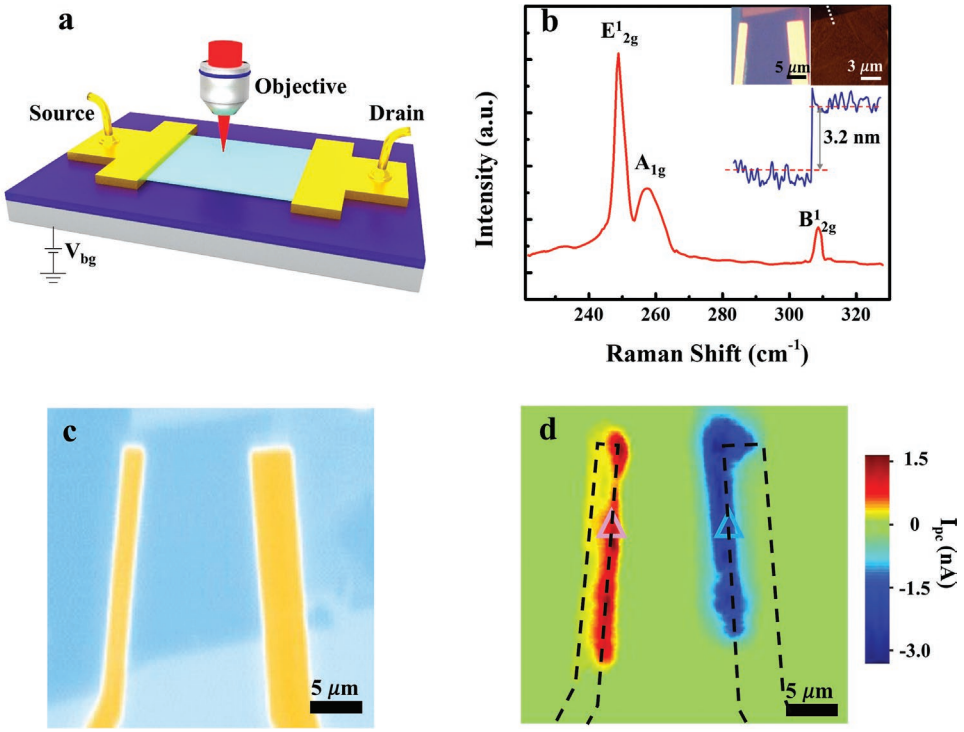

Figure 1. a) Schematic diagram of a scanning photocurrent measurement system. b) Raman spectrum of a few-layer WSe_2 flake on a SiO_2/Si substrate under 532 nm illumination. Inset: Top: Optical (left) and AFM (right) images of the WSe_2 flake. Bottom: A topographic line profile along the white dotted line in the AFM image. Reflection (c) and photocurrent (d) images of the few-layer WSe_2 transistor under 650 nm illumination with a zero gate voltage. Black dashed lines outline the Au electrodes.

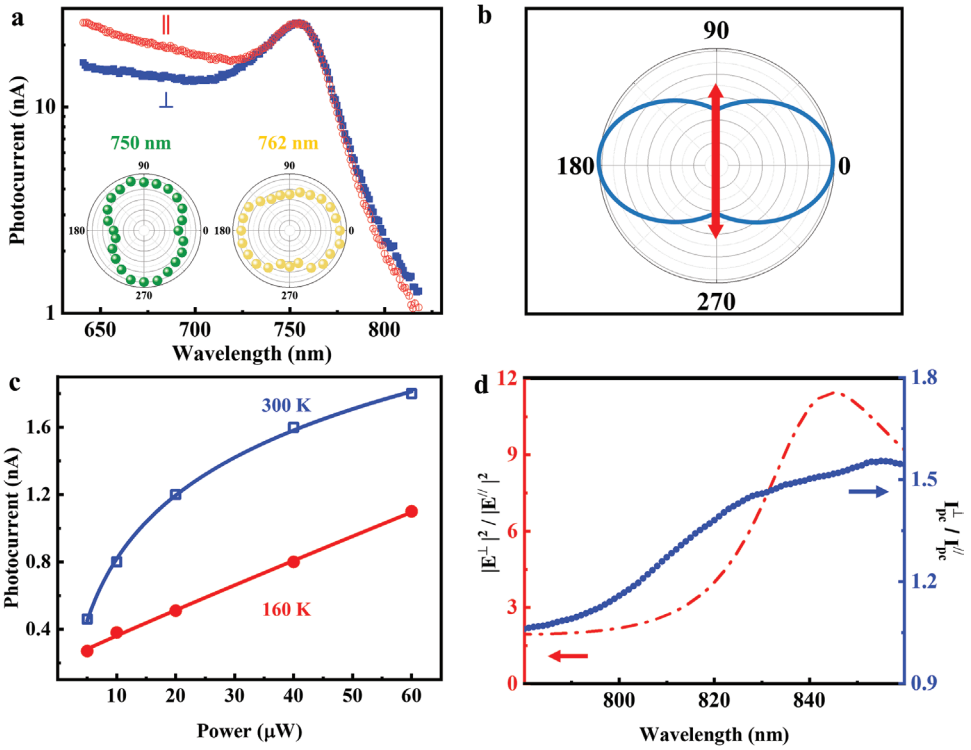

Figure 2. a) Photocurrent spectra with linearly polarized excitation at WSe_2–metal junctions under an out-of-plane voltage of 80 V. Inset: Normalized photocurrent intensity extracted from photocurrent images at WSe_2–metal junctions under 750 and 762 nm illumination, respectively. 0° is perpendicular to electrodes. b) Schematic diagram of the angular distribution function. The red arrow represents the excitation light polarization direction. c) The power dependence of the photocurrent response under 755 nm illumination at 160 K (red circle) and 300 K (blue square), respectively. d) The wavelength dependence of measured photocurrent response I_{pc} (blue) and FDTD calculated $|E|^2$ (red).

photocurrent response appears for the laser polarization direction parallel to the metal contact edge, suggesting that electrons in the valence band of WSe_2 prefer to absorb photons with the polarization direction perpendicular to their momentum direction. Such a linear polarization is similar to the optical momentum alignment effect in conventional semiconductors due to the spin-orbit interaction,[14] where two twofold-degenerate subbands of heavy and light holes are in contact at the top of the valence band. Photo-excited electrons from the heavy-hole subband show the momentum direction preferentially perpendicular to the light polarization direction, while those from the light-hole subband own the momentum direction mainly along the light polarization direction. Recently, graphene and graphene-like gapped 2D Dirac materials are theoretically predicted to exhibit similar behavior, owing to the pseudospin.[16] For WSe_2, according to Fermi's Golden Rule, the transition rate $W(\mathbf{k})$ for an electron with a wave vector $\mathbf{k}$ is given, to first-order time-dependent perturbation theory by

$$W(\mathbf{k}) = \frac{2\pi e^2 I_e}{ch\nu^2}\left|\mathbf{P}\cdot\langle\psi^c(\mathbf{k})\left|\hat{v}\right|\psi^v(\mathbf{k})\rangle\right|^2 \delta\left(E_c(\mathbf{k}) - E_v(\mathbf{k}) - h\nu\right) \quad (1)$$

Here, the ψ^C and ψ^V (E_C and E_V) are the wave functions (energies) of conduction and valence bands, respectively. $\mathbf{P}$ is the polarization vector of the incident light, which is parallel to the crystal's surface. $\hat{v}$, I_e, and ν are the velocity operator, intensity, and frequency of the incident light, respectively. Theoretical studies show that at the low energy regime the angular generation density g is

$$g = F_0(\varepsilon_0)\left[1 + \alpha_0 \cos(2\theta)\right] \quad (2)$$

where $\alpha_0 = \frac{E_g^2 - 4\varepsilon_0^2}{E_g^2 + 4\varepsilon_0^2}$ defines the degree of momentum alignment, θ is the angle between the momentum of the photo-excited electron and the polarization direction of the incident light, $F_0(\varepsilon_0)$ is the total density of carriers created at energy ε_0, and subscript 0 means that no relaxation has occurred.[16] As illustrated in Figure 2b, a linearly polarized incident light is expected to generate an anisotropic distribution of photo-excited EHPs, where the momentum direction of carriers is preferentially perpendicular to the polarization direction of incident light. Indeed, the pseudospin-related optical transition selection rules of WSe_2 induce the optical momentum alignment effect. Therefore, when the incident light is polarized in the direction along the metal edge, the photo-excited EHPs have a momentum direction perpendicular to the metal edge, which can be dissociated by the built-in electric field at the WSe_2-metal junction and thus induce photocurrent signals. In contrast, when the incident light direction is perpendicular to the metal edge, the momenta of photo-excited EHPs are along the metal edge or normal to the built-in electric field, leading to relatively weak photocurrent responses. We further study the power dependence of photocurrent response. As shown in

Figure 2c, a linear relationship with the incident light power is observed at low temperature ($I_{ph} \approx P^{\alpha}$, $\alpha = 1$), indicating that the number of photo-excited carriers is proportional to that of incident photons, whereas a sublinear behavior is displayed at room temperature ($I_{ph} \approx P^{\alpha}$, $\alpha < 1$). The sublinear relationship suggests the loss of photo-excited carriers by recombination, which may result from trap states present either in WSe_2 or at WSe_2–SiO_2 interfaces. Similar phenomena have been observed in MoS_2 and other nanomaterials.[26–28]

If the excitation photon energy is below the A exciton energy, the photocurrent signals are maximized when the polarization direction of the incident light is perpendicular to the electrode edge. These results suggest that a different photocurrent generation mechanism is involved for low-energy photon excitation. When the photon energy is lower than the A exciton energy of WSe_2, the photon cannot excite an electron from the valence band to the conduction band of WSe_2; therefore, the photocurrent signals are mainly attributed to the hot electron injection. Here, photons can be absorbed by gold electrodes to generate hot EHPs. The photo-excited hot electrons can cross over the Schottky barrier and be subsequently injected into the conduction band of WSe_2.[3,29] Therefore, the photocurrent response depends on the metal absorption (I_{ab}) that is proportional to the energy flux, which is associated to its electric field through the time-averaged Poynting vector $\langle S \rangle_{time} \sim |E|^2$. The $|E|^2$ ratio between two different polarizations can be obtained by using finite difference time domain (FDTD) simulations, as shown in Figure 2d. The calculated $|E^{\perp}|^2/|E^{\parallel}|^2$ shows a similar trend as the photocurrent measurement ($I_{pc}^{\perp}/I_{pc}^{\parallel}$), suggesting that the polarized photocurrent signal likely results from the surface plasmon resonance in metal contacts. Our experimental results suggest that due to optical momentum alignment effects, we may manipulate the polarization of the photocurrent response by shifting the A exciton peak position.

We have found that the A exciton peak can be shifted from 755 to 744 nm when an out-of-plane gate voltage is applied (**Figure 3**a). From the capacitor structure, we can estimate the electric field across the WSe_2 flakes by regarding the WSe_2 as an insulator with relative dielectric constant $\varepsilon_w = 20$ and thickness $t_w = 3.2$ nm, placing atop the silicon dioxide with relative dielectric constant $\varepsilon_{ox} = 3.9$ and thickness $t_{ox} = 300$ nm.[30–31] The electric field across the WSe_2 flake is expressed as

$$F_w = \frac{V\varepsilon_{ox}}{t_{ox}\varepsilon_w + t_w\varepsilon_{ox}} \tag{3}$$

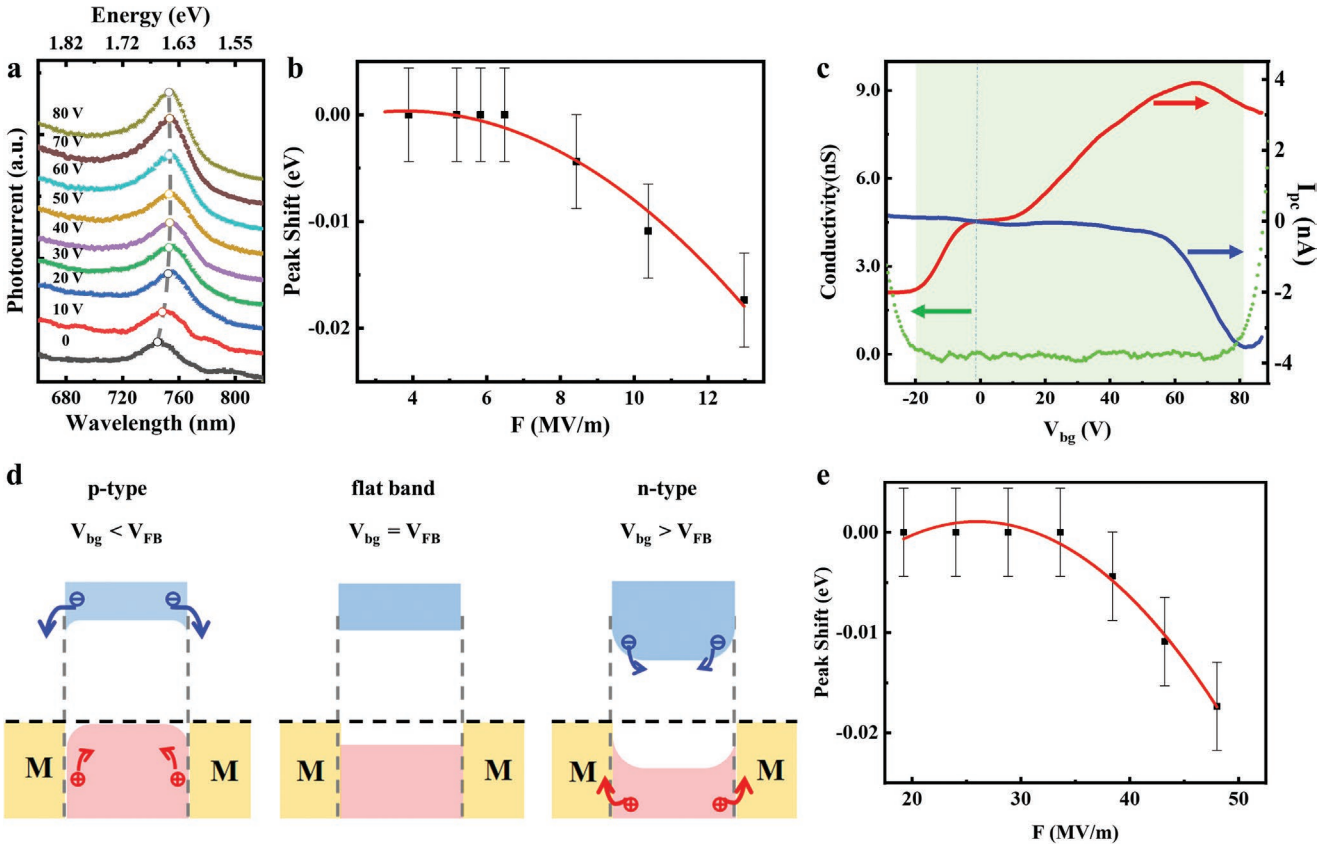

Figure 3. a) Photocurrent spectra of WSe_2-metal junctions under different gate voltages ranging from 0 to 80 V. b) Photocurrent peak shift as a function of the out-of-plane electric field, extracted from the measurements in (a). The solid red line is a parabolic fit. c) Gate-dependent photocurrent responses at red and blue triangle regions in Figure 1d and the conductivity measured as a function of the back-gate voltage. The green region shows the "off" state of the WSe_2 device. The dashed black line corresponds to $V_{bg} = V_{FB}$. d) Schematics of energy band diagrams showing photocurrent generation mechanisms under different gate voltages. e) Photocurrent peak shift as a function of an in-plane electric field based on the estimate from (c). The solid red line is a parabolic fit.

We contribute the observed shift to the quantum confined Stark effect which can modulate the interband optical transition for TMDs.[10–12] Considering the exciton as a polarizable bound EHP with a finite shift along the direction parallel to the basal plane of the crystal, the exciton recombination energy is given by:[10]

$$E(F) = E_0 - p \cdot F - \beta \cdot F^2 \quad (4)$$

where E_0 is the exciton recombination energy at $F = 0$, p is the nonzero exciton dipole moment, and β is the exciton polarizability. We extracted the polarizability $\beta \approx 3.90 \times 10^{-6}$ D m V^{-1} (Figure 3b), which s two orders of magnitude larger than the out-of-plane value obtained for MoS_2 and is comparable to those characterized via in-plane electric fields.[10–12] Here, we added the out-of-plane electric field from heavily doped silicon which could modulate the band bending at the WSe_2-Metal junction, leading to an in-plane electric field across the junction. Therefore, both in-plane and out-of-plane electric fields could influence the optical transition in WSe_2. We also performed gate-dependent scanning photocurrent measurements to estimate the in-plane electric field. By scanning the gate voltage from −30 to 90 V, the photocurrent response at the WSe_2–metal junction was recorded under 750 nm illumination (Figure 3c). When the Fermi level moves from the valence band to the conduction band, the band diagram varies linearly with a gate voltage: $\delta E_b = e\alpha V_g$, where E_b is the energy from the Fermi level to the valence band and α is a constant that shows how efficiently the gate can adjust the band energy.[32–34] The measured shut-off gate voltages for n-type and p-type conductance are 80 and −20 V, respectively (Figure 3c, green area). We also know that the indirect band gap of WSe_2 is 1.20 eV; therefore, the calculated α is about 0.012. The potential across the depletion region at the WSe_2-metal junction can be estimated as $\delta\Phi = \alpha(V_g - V_{flat})$.[35] Under illumination, photoexcited EHPs can be efficiently separated and then directed in opposite directions by built-in electric fields at WSe_2-metal junctions. For the p-type region (Figure 3d left), the electronic energies are higher in the middle of the WSe_2 device than near the contacts; therefore, electrons can be driven to the drain/source electrode, resulting in a positive/negative current. In addition, negligible photocurrent responses are observed in the middle of the device due to its relatively flat band structure. As shown in Figure 3d middle, when the gate voltage was set to −2 V, the lift of Fermi level flattened the bending in the contact region, resulting in a flat band structure. For the n-type region, an opposite polarity of photocurrent signal is detected (Figure 3d right). Based on Schottky diode electrostatics,[36] the electric field at the WSe_2-metal interface is given by $F = \delta\Phi/2w$. The depletion width w is chosen as 10 nm, since previous theoretical studies have shown that 2D material-metal junctions have a depletion region with a width about a few tens of nanometer.[37] The polarizability is calculated to be $\beta \approx 1.83 \times 10^{-6}$ D m V^{-1} (Figure 3e), which is comparable to the in-plane polarizability previously reported in monolayer TMDs.[10–12] The maximum energetic shift $\Delta E_{max} \approx -25$ meV is much smaller than the exciton binding energy of WSe_2,[38] since the electric field only weakly perturbs the oscillator strength of the transition.

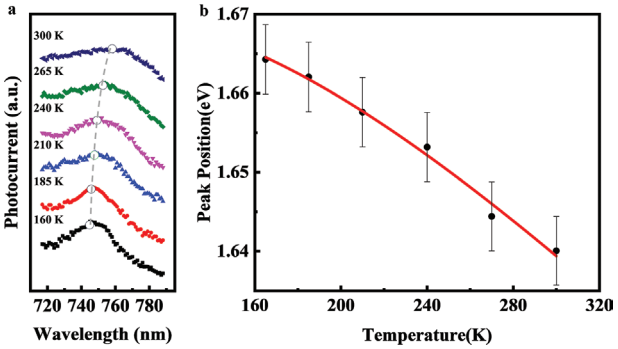

Figure 4. a) Photocurrent spectra of WSe_2-metal junctions at various temperatures ranging from 160 to 300 K. b) Photocurrent peak shift as a function of temperature, extracted from the measurements in (a). The solid red line is a fit to the data using a modified Varshni's equation.

We also notice that the photocurrent response peak can be shifted by environmental temperatures (**Figure 4**a). We extracted the peak position at each temperature (Figure 4b) and fit it to a modified Varshni's equation:[39]

$$E_g(T) = E_g(0) - S\langle\hbar\omega\rangle\left[\coth\left(\frac{\langle\hbar\omega\rangle}{2k_BT}\right) - 1\right] \quad (5)$$

where $E_g(0)$ is the band gap at 0 K, S is a dimensionless electron-phonon coupling parameter, $\langle\hbar\omega\rangle$ is the average acoustic phonon energy involved in electron-phonon interactions. From the fitting in Figure 4b, $S \approx 1.67$ and $E_g(0) = 1.73$ eV are extracted for A exciton, respectively. We notice that $E_g(0)$ is comparable to that of monolayer WSe_2 (1.74 eV), while S is smaller than previous reports for monolayer WSe_2 (2.06 or 2.33).[39,40] This indicates that the electron-phonon coupling in few-layer WSe_2 is weaker than that in its monolayer structure, likely due to the increased effective mass from monolayer to few-layer WSe_2.[40] As we increase the temperature, the A exciton energy of WSe_2 becomes smaller, leading to the peak shift of photocurrent spectra at various temperatures. These studies may provide a new strategy to modulate the polarization direction of photocurrent responses in WSe_2 by shifting its A exciton energy via temperature.

3. Conclusion

In conclusion, we systematically investigate the photocurrent generation mechanisms at the WSe_2-metal junctions via wavelength-, polarization-, gate-, and temperature-dependent scanning photocurrent measurements. We find that if the photon energy is above the A exciton energy, the maximum photocurrent response appears for the light polarization direction along the metal electrode edge, suggesting that electrons in the valence band of WSe_2 tend to obtain photons with the polarization direction perpendicular to their momentum direction. Such a linear polarization behavior is known as the optical momentum alignment effect because of the pseudospin-induced optical selection rule. Similar behavior has been widely studied in conventional semiconductors. If the photon energy is lower than the A exciton energy, the photocurrent signals

are maximized when the polarization direction of the incident light is perpendicular to the metal electrode edge, which mainly result from hot electrons generated by the polarized absorption of the gold electrodes due to surface plasmon resonances. More interestingly, the photocurrent peak can be modulated by either an external electric field or environmental temperature. These experimental studies provide an in-depth understanding of photocurrent generation mechanisms, offering new design rules for future 2D TMD-based anisotropic optoelectronics.

4. Experimental Section

Device Fabrication: To enhance hydrophilicity, degenerately p-doped silicon substrates with 300 nm of SiO_2 were treated by oxygen plasma for 5 min. The substrates were then bath sonicated in acetone, isopropyl alcohol for about 10 min. WSe_2 flakes were mechanically exfoliated from WSe_2 crystals (2D semiconductors) onto the pre-cleaned substrates. Optical microscopy, Raman microscopy, and AFM were used to identify WSe_2 flakes. The metal contacts were fabricated by electron beam lithography and then deposited by electron beam evaporation of Cr (5 nm) and Au (40 nm).

Scanning Photocurrent Measurements: A NKT Photonic SuperK Supercontinuum laser system was utilized to provide a linearly-polarized continuous wave laser beam, which was focused into a diffraction limited spot (≈1 μm) by a 40X Olympus objective. Its polarization direction was controlled via a half-wave plate and then followed by a polarizer. A nanometer-resolution scan mirror was used to change its position. The photocurrent signals were collected by a preamplifier, while the reflection of the incident laser light was measured by a Si photodetector to locate the position of the device. All experimental were performed in a Janis ST-500cryostat under vacuum ($\approx 1 \times 10^{-6}$ Torr).

FDTD Simulation: The $|E|^2$ ratio was obtained via 3D finite difference time domain simulations (Lumerical FDTD Solutions). The geometries were taken based on the device dimensions. The light source was a plane wave and the mesh size was 4 nm. The optical field at the interface between electrodes and the underlying SiO_2 was recorded by frequency domain field and power monitors. To collect the optical field within 1 μm from the edges of electrodes, the width of the optical field monitors was chosen to be 2 μm wider than the electrodes.

Acknowledgements

This work was supported by the National Science Foundation (ECCS-1810088 and CBET-1805924).

Conflict of Interest

The authors declare no conflict of interest.

Data Availability Statement

The data that support the findings of this study are available from the corresponding author upon reasonable request.

Keywords

optical momentum alignment effect, quantum confined Stark effect, scanning photocurrent microscopy, temperature, WSe_2

Received: December 26, 2020
Revised: March 19, 2021
Published online: April 23, 2021

[1] L. Yang, N. A. Sinitsyn, W. Chen, J. Yuan, J. Zhang, J. Lou, S. A. Crooker, *Nat. Phys.* **2015**, *11*, 830.
[2] R. Suzuki, M. Sakano, Y. Zhang, R. Akashi, D. Morikawa, A. Harasawa, K. Yaji, K. Kuroda, K. Miyamoto, T. Okuda, *Nat. Nanotechnol.* **2014**, *9*, 611.
[3] T. Hong, B. Chamlagain, S. Hu, S. M. Weiss, Z. Zhou, Y.-Q. Xu, *ACS Nano* **2015**, *9*, 5357.
[4] Y. Zhang, T.-R. Chang, B. Zhou, Y.-T. Cui, H. Yan, Z. Liu, F. Schmitt, J. Lee, R. Moore, Y. Chen, H. Lin, H.-T. Jeng, S.-K. Mo, Z. Hussain, A. Bansil, Z.-X. Shen, *Nat. Nanotechnol.* **2013**, *9*, 111.
[5] W. Zhao, R. M. Ribeiro, M. Toh, A. Carvalho, C. Kloc, A. H. Castro Neto, G. Eda, *Nano Lett.* **2013**, *13*, 5627.
[6] J. Gusakova, X. Wang, L. L. Shiau, A. Krivosheeva, V. Shaposhnikov, V. Borisenko, V. Gusakov, B. K. Tay, *Phys. Status Solidi A* **2017**, *214*, 1700218.
[7] Y. Ye, J. Xiao, H. Wang, Z. Ye, H. Zhu, M. Zhao, Y. Wang, J. Zhao, X. Yin, X. Zhang, *Nat. Nanotechnol.* **2016**, *11*, 598.
[8] G. Plechinger, P. Nagler, A. Arora, R. Schmidt, A. Chernikov, A. G. Del Águila, P. C. Christianen, R. Bratschitsch, C. Schüller, T. Korn, *Nat. Commun.* **2016**, *7*, 12715.
[9] J. Kim, C. Jin, B. Chen, H. Cai, T. Zhao, P. Lee, S. Kahn, K. Watanabe, T. Taniguchi, S. Tongay, *Sci. Adv.* **2017**, *3*, e1700518.
[10] J. Klein, J. Wierzbowski, A. Regler, J. Becker, F. Heimbach, K. Müller, M. Kaniber, J. J. Finley, *Nano Lett.* **2016**, *16*, 1554.
[11] J. G. Roch, N. Leisgang, G. Froehlicher, P. Makk, K. Watanabe, T. Taniguchi, C. Schönenberger, R. J. Warburton, *Nano Lett.* **2018**, *18*, 1070.
[12] M. Massicotte, F. Vialla, P. Schmidt, M. B. Lundeberg, S. Latini, S. Haastrup, M. Danovich, D. Davydovskaya, K. Watanabe, T. Taniguchi, *Nat. Commun.* **2018**, *9*, 1633.
[13] D. A. Miller, D. Chemla, T. Damen, A. Gossard, W. Wiegmann, T. Wood, C. Burrus, *Phys. Rev. Lett.* **1984**, *53*, 2173.
[14] B. P. Zakharchenya, D. N. Mirlin, V. Perel', I. Reshina, *Phys. Usp.* **1982**, *25*, 143.
[15] X. Y. Peng, Q. Zhang, B. Shen, J. R. Shi, C. M. Yin, X. W. He, F. J. Xu, X. Q. Wang, N. Tang, C. Y. Jiang, Y. H. Chen, K. Chang, *Phys. Rev. B* **2011**, *84*, 075341.
[16] V. Saroka, R. Hartmann, M. Portnoi, *arXiv:1811.00987* **2018**.
[17] M. A. Hossain, J. Yu, A. M. van der Zande, *ACS Appl. Mater. Interfaces* **2020**, *12*, 48910.
[18] K. Thakar, S. Lodha, *Mater. Res. Express* **2020**, *7*, 014002.
[19] T. Wang, K. Andrews, A. Bowman, T. Hong, M. Koehler, J. Yan, D. Mandrus, Z. Zhou, Y.-Q. Xu, *Nano Lett.* **2018**, *18*, 2766.
[20] C. D. Ornelas, A. Bowman, T. S. Walmsley, T. Wang, K. Andrews, Z. Zhou, Y.-Q. Xu, *ACS Appl. Mater. Interfaces* **2020**, *12*, 46476.
[21] Y. Yang, J. Jeon, J.-H. Park, M. S. Jeong, B. H. Lee, E. Hwang, S. Lee, *ACS Nano* **2019**, *13*, 8804.
[22] Y. Tang, Z. Wang, P. Wang, F. Wu, Y. Wang, Y. Chen, H. Wang, M. Peng, C. Shan, Z. Zhu, S. Qin, W. Hu, *Small* **2019**, *15*, 1805545.
[23] T. S. Walmsley, K. Andrews, T. Wang, A. Haglund, U. Rijal, A. Bowman, D. Mandrus, Z. Zhou, Y.-Q. Xu, *Nanoscale* **2019**, *11*, 14410.
[24] P. Tonndorf, R. Schmidt, P. Böttger, X. Zhang, J. Börner, A. Liebig, M. Albrecht, C. Kloc, O. Gordan, D. R. T. Zahn, S. Michaelis de Vasconcellos, R. Bratschitsch, *Opt. Express* **2013**, *21*, 4908.
[25] W. J. Zhao, Z. Ghorannevis, L. Q. Chu, M. L. Toh, C. Kloc, P. H. Tan, G. Eda, *ACS Nano* **2013**, *7*, 791.
[26] O. Lopez-Sanchez, D. Lembke, M. Kayci, A. Radenovic, A. Kis, *Nat. Nanotechnol.* **2013**, *8*, 497.
[27] W. Zhang, J.-K. Huang, C.-H. Chen, Y.-H. Chang, Y.-J. Cheng, L.-J. Li, *Adv. Mater.* **2013**, *25*, 3456.
[28] F. González-Posada, R. Songmuang, M. Den Hertog, E. Monroy, *Nano Lett.* **2011**, *12*, 172.
[29] T. Wang, Y.-Q. Xu, *Electronics* **2016**, *5*, 93.

[30] A. D. Mohite, P. Gopinath, H. M. Shah, B. W. Alphenaar, *Nano Lett.* **2008**, *8*, 142.
[31] Y. Li, A. Chernikov, X. Zhang, A. Rigosi, H. M. Hill, A. M. van der Zande, D. A. Chenet, E.-M. Shih, J. Hone, T. F. Heinz, *Phys. Rev. B* **2014**, *90*, 205422.
[32] S. Rosenblatt, Y. Yaish, J. Park, J. Gore, V. Sazonova, P. L. McEuen, *Nano Lett.* **2002**, *2*, 869.
[33] Y. Ahn, J. Dunning, J. Park, *Nano Lett.* **2005**, *5*, 1367.
[34] M. Freitag, J. C. Tsang, A. Bol, D. Yuan, J. Liu, P. Avouris, *Nano Lett.* **2007**, *7*, 2037.
[35] T. Hong, B. Chamlagain, W. Lin, H.-J. Chuang, M. Pan, Z. Zhou, Y.-Q. Xu, *Nanoscale* **2014**, *6*, 8978.
[36] E. H. Rhoderick, *IEE Proc. I – Solid-State Electron. Devices* **1982**, *129*, 1.
[37] A. Nipane, S. Jayanti, A. Borah, J. T. Teherani, *J. Appl. Phys.* **2017**, *122*, 194501.
[38] X. Xu, W. Yao, D. Xiao, T. F. Heinz, *Nat. Phys.* **2014**, *10*, 343.
[39] A. Arora, M. Koperski, K. Nogajewski, J. Marcus, C. Faugeras, M. Potemski, *Nanoscale* **2015**, *7*, 10421.
[40] J. Huang, T. B. Hoang, M. H. Mikkelsen, *Sci. Rep.* **2016**, *6*, 22414.